ELSEVIER

Volume 180, Number 3, March 2007

JOURNAL OF SOLID STATE CHEMISTRY

www.elsevier.com/locate/jssc

CONTENTS

Abstracted/indexed in BioEngineering Abstracts, Chemical Abstracts, Coal Abstracts, Current Contents/Physics, Chemical, & Earth Sciences, Engineering Index, Research Alert, SCISEARCH, Science Abstracts, and Science Citation Index. Also covered in the abstract and citation database SCOPUS®. Full text available on ScienceDirect®.

Regular Articles

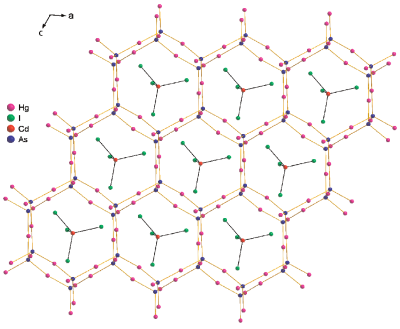

A new quaternary supramolecular complex $(Hg_2As)_2(CdI_4)$ (**1**) has been prepared by the solid-state reaction, and structurally characterized by single crystal X-ray diffraction analysis. The structure of **1** is characterized by a 3-D tridymite-like cationic framework with the channels being occupied by discrete CdI_4^{2-} tetrahedral guest-anions.

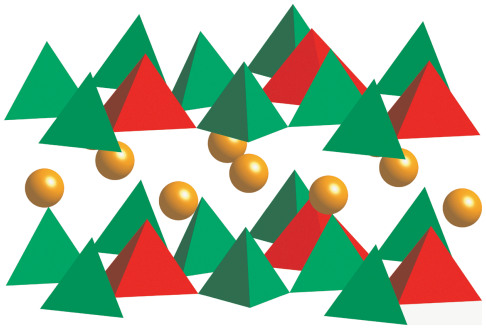

The 115 K phase transition in the fresnoite-type $K_2V_3O_8$ is elucidated by neutron powder and single-crystal X-ray diffraction. Below 115 K, weak superlattice reflections are clearly evident in X-ray diffraction patterns recorded by a CCD detector, and these extra reflections can be indexed with the wave vector $\pm 1/3\langle 110\rangle^* + 1/2c^*$.

Regular Articles—Continued

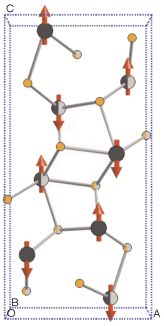

The spin-dependent EHTB method correctly predicts the magnetic structure of α-Gd_2S_3 determined from neutron diffraction experiments.

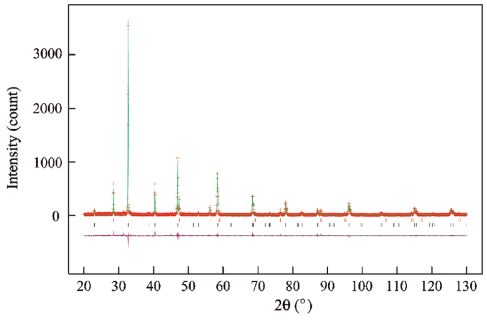

X-ray diffraction data and calculated pattern for $Na_{1/2}La_{1/2}TiO_3$, the end-member of the $Ca_{1-2x}Na_xLa_xTiO_3$ $(x = 0.5)$. The experimental data are shown as crosses, the calculated fits and difference curves as solid lines. Tick marks (upper row for internal standard silicon) indicate the calculated positions of peaks.

Crystal structure and magnetic properties of the solid-solution phase $Ca_3Co_{2-v}Sc_vO_6$

Charles H. Hervoches, Vivian Miksch Fredenborg, Arne Kjekshus, Helmer Fjellvåg and Bjørn C. Hauback

Page 834

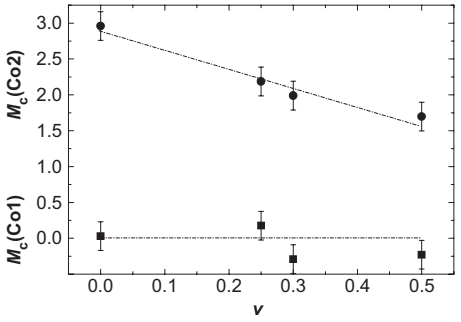

The quasi-one-dimensional $Ca_3Co_2O_6$ phase forms a substitutional solid-solution system with Sc, in which the Sc atoms enter the Co2 sublattice exclusively. The homogeneity range of $Ca_3Co_{2-v}Sc_vO_6$ extends up to $v \approx 0.55$. The magnetic moment decreases rapidly with increasing amount of the non-magnetic Sc solute in the lattice.

Synthesis and characterization of mixed-morphology $CePO_4$ nanoparticles

L. Karpowich, S. Wilcke, Rong Yu, G. Harley, J.A. Reimer and L.C. De Jonghe

Page 840

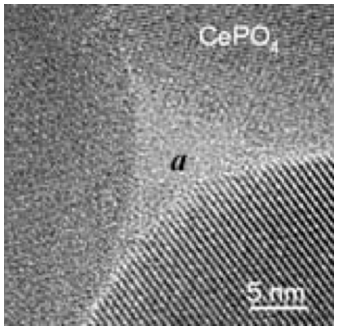

High resolution electron microscopy image of amorphous intergranular phase (a) in polycrystalline monazite $CePO_4$.

Enthalpies of formation of rare earth orthovanadates, *RE*VO_4

M. Dorogova, A. Navrotsky and L.A. Boatner

Page 847

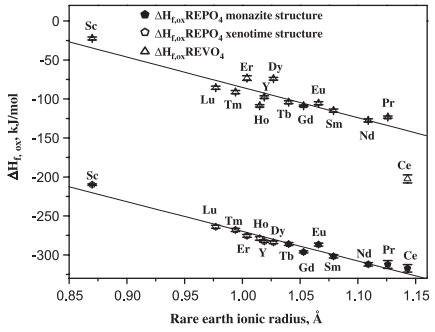

Comparison of enthalpies of formation from oxides at 298 K for *RE*VO_4 [this work] and *RE*PO_4 compounds [S.V. Ushakov, K.B. Helean, A. Navrotsky, L.A. Boatner, J. Mater. Res. 16(9) (2001) 2623] vs. RE^{3+} ionic radius. Filled symbols indicate scheelite structure, open symbols zircon structure.

$Zr_{1-x}Ln_xW_2O_{8-x/2}$ (Ln = Eu, Er, Yb): Solid solutions of negative thermal expansion-synthesis, characterization and limited solid solubility

Hai-Hua Li, Jing-Sa Han, Hui Ma, Ling Huang and Xin-Hua Zhao

Page 852

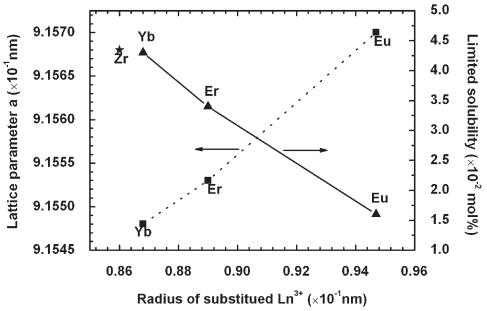

The graphic displays the lattice parameters of saturated solid solutions and solubility of $Zr_{1-x}Ln_xW_2O_{8-y}$ as a function of the radius of substituted Ln^{3+} ions. A more sensitive method is developed to measure the low solubility of the solid solutions. This correlation demonstrates the increase in limited solid solubility follows the lanthanide contraction trend in a way that is opposite to that observed for lattice parameters.

Structured diffuse scattering and polar nano-regions in the $Ba(Ti_{1-x}Sn_x)O_3$ relaxor ferroelectric system

Yun Liu, Ray L. Withers, Xiaoyong Wei and John D. Fitz Gerald

Page 858

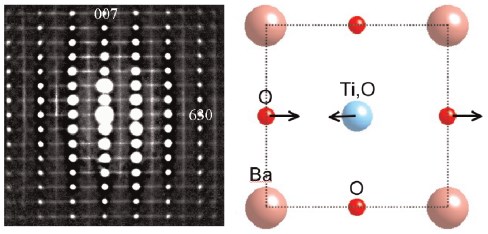

The characteristic $\mathbf{G} \pm \{001\}^*$ sheets of diffuse intensity characteristic of the relaxor ferroelectric $Ba(Ti_{1-x}Sn_x)O_3$ (BTS), $0.1 \leqslant x \leqslant 0.5$, system along with the inherently polar, transverse optical modes of distortion responsible.

Three-dimensional framework of uranium-centered polyhedra with non-intersecting channels in the uranyl oxy-vanadates $A_2(UO_2)_3(VO_4)_2O$ (A = Li, Na)

S. Obbade, L. Duvieubourg, C. Dion and F. Abraham

Page 866

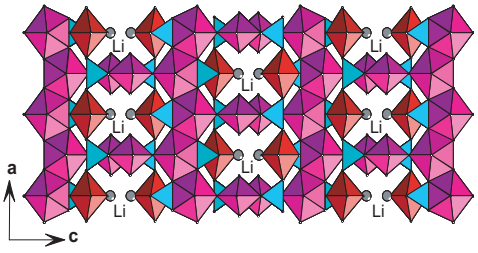

A view of the 3-D structure of $Li_2(UO_2)_3(VO_4)_2O$.

Continued

Stabilization of Co^{2+} in layered double hydroxides (LDHs) by microwave-assisted ageing

M. Herrero, P. Benito, F.M. Labajos and V. Rives

Page 873

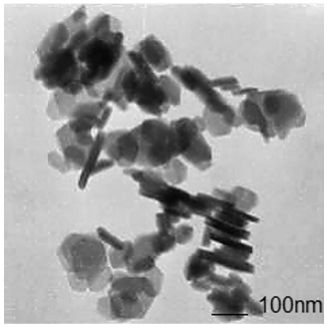

The use of microwave-hydrothermal treatment, controlling both temperature and ageing time, permits to synthesize well-crystallized nanomaterials with controlled surface properties. An enhancement in the crystallinity degree and an increase in the particle size are observed when the irradiation time is prolonged.

TEM investigation of the microporous compound VSB-1: Building units and crystal growth mechanisms

Marie Colmont and Osamu Terasaki

Page 885

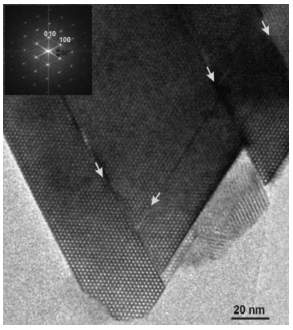

TEM investigation of the microporous compound VSB-1 evidenced defects and information about building units and crystal growth. As usually observed for microporous materials, the crystal growth via a layer by layer mechanism.

Effect of sorbed molecules on the resistivity of alkali metal–graphite intercalation compounds

Noboru Akuzawa, Yoji Kunihashi, Yuki Sato, Ken-ichi Tsuchiya and Rika Matsumoto

Page 894

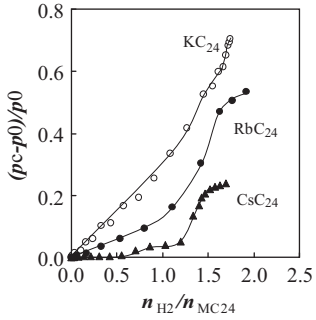

The resistivity of MC_{24} increased with increase of the sorbed amount of H_2. The magnitude of the increase was in the order $KC_{24} > RbC_{24} > CsC_{24}$. This resistivity increase was considered to be due to the expansion along *c*-direction which reduces the charge-transfer interaction between the carbon layers and potassium ions.

Preparation of mesoporous cadmium sulfide nanoparticles with moderate pore size

Zhaohui Han, Huaiyong Zhu, Jeffrey Shi, Gordon Parkinson and G.Q. Lu

Page 902

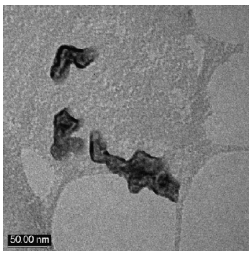

The preparation involves a hydrothermal process and a subsequent acid treatment process, the majority of the particles have a moderate pore size, which complements and fills the gap between existing porous materials usually have a pore size either less than 10 nm or well above 100 nm.

$$ZnCl_2 + NaOH + NaHS \cdot xH_2O \xrightarrow[\text{Hydrothermal process}]{CdCl_2}$$

$$Zn_5(OH)_5Cl_2 \cdot H_2O/Cd_{7.23}Zn_{2.7}S_{10} + ZnO/Cd_{7.23}Zn_{2.7}S_{10} \xrightarrow{\text{Dilute HCl}}$$

Porous CdS.

Growth of new ternary intermetallic phases from Ca/Zn eutectic flux

Milorad Stojanovic and Susan E. Latturner

Page 907

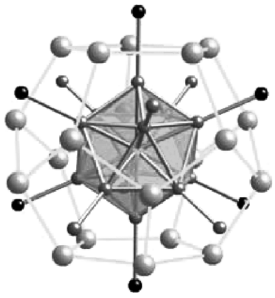

The calcium/zinc eutectic is a useful synthesis medium for the growth of new intermetallic phases. Addition of group 10 transition metals to this flux produces ternary phases $CaNi_2Zn_3$, $Ca_{21}Ni_2Zn_{36}$, $CaPd_{0.85}Zn_{1.15}$, and $Ca_6Pt_3Zn_5$. The nickel-centered zinc icosahedron surrounded by a pentagonal dodecahedron of calcium atoms is found in $Ca_{21}Ni_2Zn_{36}$.

Defect structure of $Sb_{2-x}Fe_xTe_3$ single crystals

J. Horák, P. Lošťák, Č. Drašar, J. Navrátil and C. Uher

Page 915

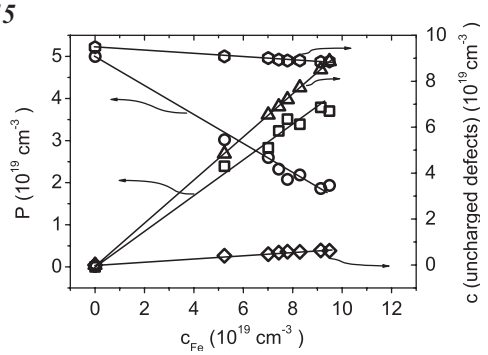

The concentration of holes *P* and the concentration of defects *c* in $Sb_{2-x}Fe_xTe_3$ single crystals on Fe-content.

$Li_2Si_3O_7$: Crystal structure and Raman spectroscopy
Hannes Krüger, Volker Kahlenberg and Reinhard Kaindl
Page 922

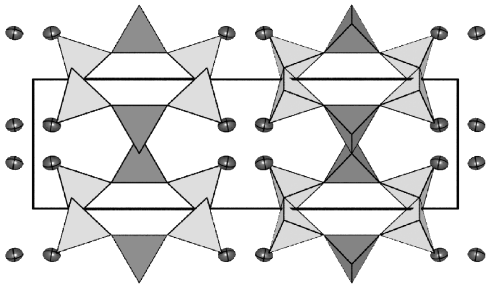

Structure of $Li_2Si_3O_7$: $[Si_6O_{14}]$ silicate layers formed by two independent *zweier* single chains. Lithium atoms represented by 95% probability displacement ellipsoids.

Synthesis and characterization of new strontium 4-carboxyphenylphosphonates
Vítězslav Zima, Jan Svoboda, Ludvík Beneš, Klára Melánová, Miroslava Trchová and Jiří Dybal
Page 929

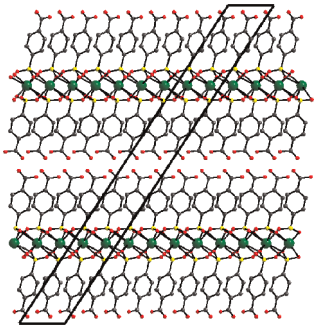

The structure of β-$Sr(HOOCC_6H_4PO_3H)_2$ viewed in the direction of the the *bc* plane.

Comparative high-pressure study and chemical bonding analysis of Rh_3Bi_{14} and isostructural $Rh_3Bi_{12}Br_2$
Q.F. Gu, G. Krauss, Yu. Grin and W. Steurer
Page 940

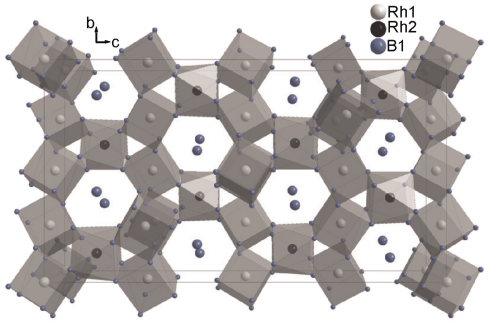

Rh_3Bi_{14} isostructural with $Rh_3Bi_{12}Br_2$ consists of a 3D framework of edge-sharing cubes and square antiprisms. High-pressure X-ray powder diffraction measurements of Rh_3Bi_{14} and $Rh_3Bi_{12}Br_2$ indicate a high stability of both compounds in the investigated range from ambient pressure to ca 30 GPa at room temperature.

Synthesis and characterizations of hierarchical biomorphic titania oxide by a bio-inspired bottom-up assembly solution technique
Qun Dong, Huilan Su, Wei Cao, Di Zhang, Qixin Guo and Yijian Lai
Page 949

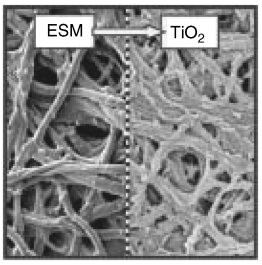

Hierarchical mesoporous TiO_2 is assembled by nanoparticles from the nanoscale to the macroscale through a bio-inspired sol–gel approach with eggshell membrane used as the biotemplate. As-prepared hierarchical titania shows porous characters within the pore size range of 2 nm–4 μm.

Crystal chemistry of $M[PO_2(OH)_2]_2 \cdot 2H_2O$ compounds (M = Mg, Mn, Fe, Co, Ni, Zn, Cd): Structural investigation of the Ni, Zn and Cd salts
Violeta Koleva and Herta Effenberger
Page 956

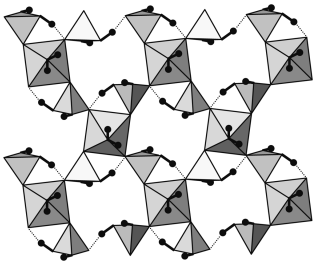

IR spectroscopy showed the internal PO_4 vibrations to be insensitive to the size and the electronic configuration of the M^{2+} ions and reflect the more ionic character of the Mg–O bonds. The observed "*ABC* trio" characteristic for acidic salts is discussed. Single-crystal X-ray investigations were performed at 120 and 295 K. One of the four hydrogen bonds is worth mentioning because of the short $O_h \cdots O$ bond distance of 2.57–2.61 Å at room temperature (2.56–2.57 Å at 120 K).

Experimental and theoretical contributions to the determination of optical properties of synthetic paramelaconite
J.F. Pierson, E. Duverger and O. Banakh
Page 968

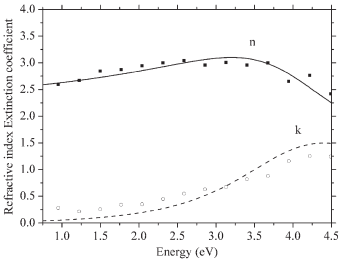

Comparison between experimental (lines) and calculated (points) refractive index and extinction coefficient values. For experimental measurements, the film was deposited on silicon substrate.

Continued

Single-crystal synthesis, structure analysis, and physical properties of the calcium ferrite-type $Na_xTi_2O_4$ with $0.558 < x < 1$

Yasuhiko Takahashi, Kunimitsu Kataoka, Ken-ichi Ohshima, Norihito Kijima, Junji Awaka, Kenji Kawaguchi and Junji Akimoto

Page 1020

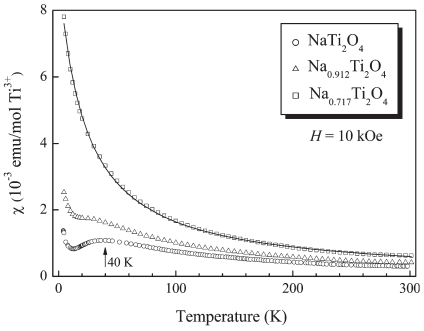

Magnetic susceptibility of three $Na_xTi_2O_4$ samples below 300 K. The broad maximum around 40 K observed in as-grown $NaTi_2O_4$ is suppressed by an Na deficiency and vanishes in $Na_{0.717}Ti_2O_4$.

Large aspect ratio titanate nanowire prepared by monodispersed titania submicron sphere via simple wet-chemical reactions

Baoxiang Wang, Yong Shi and Dongfeng Xue

Page 1028

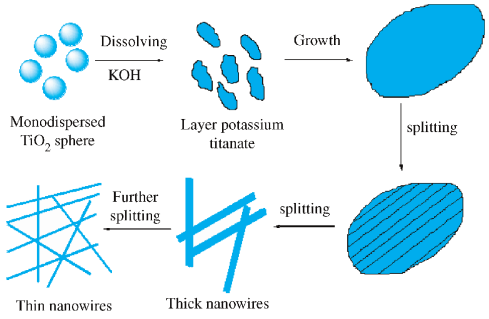

Monodispersed raw titania powders are beneficial to get the long and uniform $K_2Ti_6O_{13}$ nanowires with a large aspect ratio. A formation mechanism of nanowires is proposed based on the dissolving, growth, thickening and splitting of $K_2Ti_6O_{13}$ nano-intermediates.

Magnetic diphase nanostructure of $ZnFe_2O_4/\gamma$-Fe_2O_3

Xiangxi Bo, Guangshe Li, Xiaoqing Qiu, Yanfeng Xue and Liping Li

Page 1038

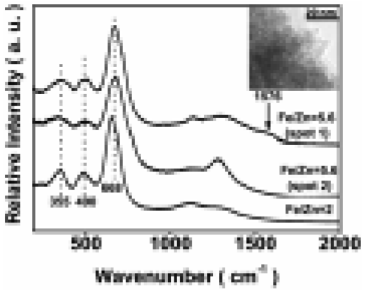

Spherical diphase nanostructure of $ZnFe_2O_4/\gamma$-Fe_2O_3 was obtained by varying the initial molar ratio of Fe/Zn.

Crystal structure, phase relations and electrochemical properties of monoclinic Li_2MnSiO_4

V.V. Politaev, A.A. Petrenko, V.B. Nalbandyan, B.S. Medvedev and E.S. Shvetsova

Page 1045

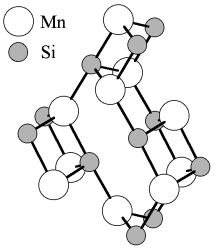

Arrangement of Mn (large white balls) and Si (small grey balls) atoms in Li_2MnSiO_4 structure. Bold lines connect atoms linked via common oxygen (not shown).

Crystal structure and magnetic properties of two new cobalt selenite halides: $Co_5(SeO_3)_4X_2$ (X = Cl, Br)

Richard Becker, Mladen Prester, Helmuth Berger, Ping Hui Lin, Mats Johnsson, Djuro Drobac and Ivica Zivkovic

Page 1051

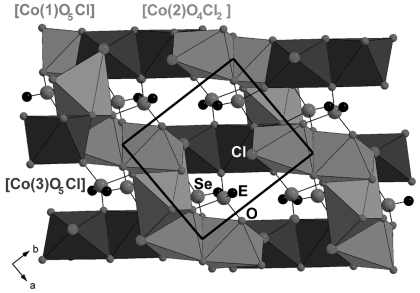

Two new iso-structural cobalt selenite halides $Co_5(SeO_3)_4Cl_2$ and $Co_5(SeO_3)_4Br_2$ have been synthesized which are iso-structural to $Ni_5(SeO_3)_4Br_2$. Magnetic susceptibility measurements on oriented single-crystalline samples show anisotropic response in a broad temperature range, revealing significant single-ion anisotropy effects.

Structure and basic magnetic properties of the honeycomb lattice compounds $Na_2Co_2TeO_6$ and $Na_3Co_2SbO_6$

L. Viciu, Q. Huang, E. Morosan, H.W. Zandbergen, N.I. Greenbaum, T. McQueen and R.J. Cava

Page 1060

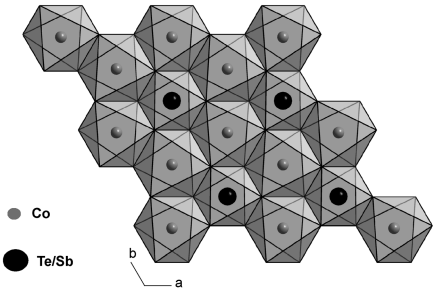

The layer of edge-shared MO_6 octahedra, showing the honeycomb Co array.

Continued

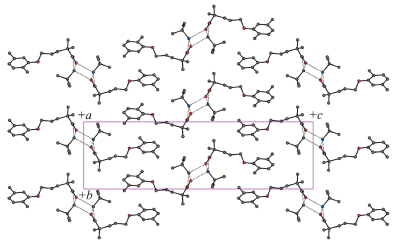

Structural properties of a family of co-crystals containing gemfibrozil and hydroxy derivatives of *t*-butylamine are discussed and rationalized.

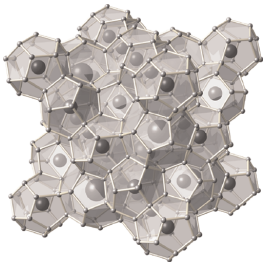

The synthesis of framework-substituted type II germanium clathrates, $Cs_8Na_{16}Ag_xGe_{136-x}$, is reported for the first time. Single crystal X-ray diffraction studies indicate that Ag substitutes for Ge on the clathrate framework, with preferential substitution occurring on the 96*g* site. These results offer new direction in the synthesis of novel clathrate compounds, materials of interest for potential thermoelectric applications.

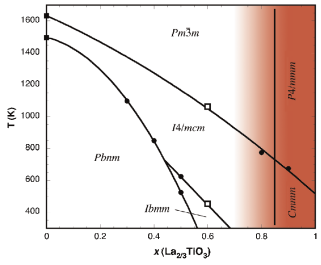

Phase diagram for $Ca_{(1-x)}La_{3x/2}TiO_3$ based on transition temperatures obtained from *in situ* neutron and synchrotron X-ray powder diffraction studies: depending on whether or not we have in-phase and/or out-of-phase octahedral tilting, whether we have long-range cation/vacancy ordering (the degree of ordering is indicated by shading), six distinct structures occur.

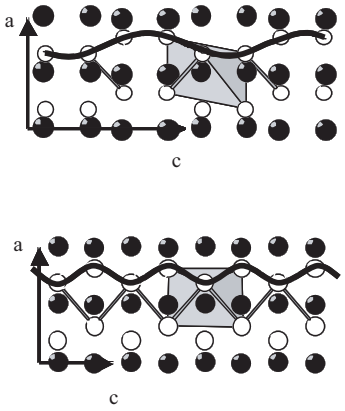

The NiP (top) and NiGe (bottom) crystal structures. The structural relationship is emphasised by indicating the xsin[Ge/P] modulation wave in the 4-d space group setting *Amam*(0 0 γ)s00; $\gamma = 1$ for NiGe, $\gamma = 1/2$ for NiP and $0.78 < \gamma < 0.70$ for $NiGe_{1-x}P_x$ with $0.4 > x > 0.7$.

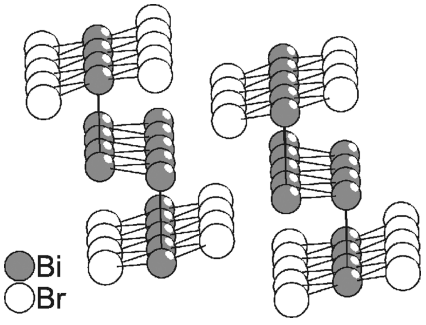

Quasi one-dimensional compounds Bi_4Br_4 and Bi_4I_4 have been investigated theoretically (electronic structure calculations) and experimentally (galvanomagnetic and magnetic measurements). Both compounds are found to be diamagnetic, room-temperature semiconductors with n-type conductivity and a possibility of significant directional anisotropy. Magnetoresistivity data indicate some weak interactions between isolated bismuth fragments in Bi_4I_4.

$AgGaS_2$-type photocatalysts for hydrogen production under visible light: Effects of post-synthetic H_2S treatment

Jum Suk Jang, Sun Hee Choi, Namsoo Shin, Chungjong Yu and Jae Sung Lee

Page 1110

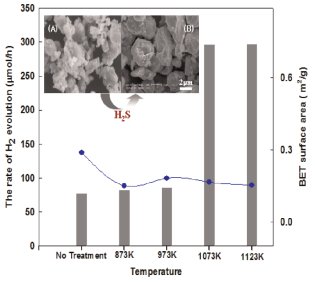

Post-treatment of $AgGaS_2$ under H_2S flow at 1123 K resulted in the well-defined chalcopyrite structure, which was revealed mainly by Rietveld analysis of XRD and detailed EXAFS study. The diameters of $AgGaS_2$ particles treated at 873–1123 K under H_2S gas flow are ca. 2–3 nm, almost the same as that of H_2S-untreated material. In untreated sample, $AgGaS_2$ particles were surrounded by the broken powders having sharp edges. But there were almost no broken particles and the surface became smoother for $AgGaS_2$ treated with H_2S gas at 1123 K. The rates of hydrogen evolution over H_2S treated $AgGaS_2$ at higher temperatures (1073 and 1123 K) were higher than those of photocatalysts untreated or treated at lower temperatures (873, 973 K). There is almost no correlation between BET surface areas and hydrogen evolution rates.

Sulfur radicals embedded in various cages of ultramarine analogs prepared from zeolites

Stanisław Kowalak, Aldona Jankowska, Sebastian Zeidler and Andrzej B. Więckowski

Page 1119

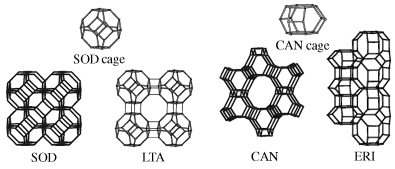

Structures of SOD, LTA, cancrinite and erionite.

Intercalation behavior of *n*-alkylamines into an *A*-site defective layered perovskite $H_2W_2O_7$

Bingshan Wang, Xiaowen Dong, Qingyi Pan, Zhixuan Cheng and Yanze Yang

Page 1125

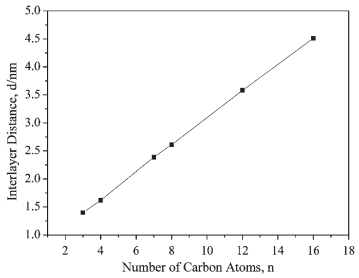

$H_2W_2O_7$ can accommodate *n*-alkylamines ($C_nH_{2n+1}NH_2$: $n = 3$, 4, 7, 8, 12, 16) to form intercalation compounds via an acid–base mechanism. After intercalation, the [001] reflections of $H_2W_2O_7$ shift to lower angles. The basal space of the intercalation products with *n*-alkylamines increases with an increase of the number of carbon atoms in *n*-alkyl chain. The relationship between the interlayer distance, *d* and the number of carbon atoms in the *n*-alkyl chain, *n*, is demonstrated in figure. A linear relationship is clearly observed, as expressed with $d = 0.241n + 0.67$.

Characterization and acidic properties of Al-SBA-15 materials prepared by post-synthesis alumination of a low-cost ordered mesoporous silica

M. Gómez-Cazalilla, J.M. Mérida-Robles, A. Gurbani, E. Rodríguez-Castellón and A. Jiménez-López

Page 1130

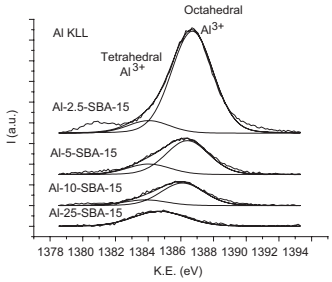

Al KLL spectra of Al-SBA-15 materials with different Si/Al ratios.

A new molecular precursor route for the synthesis of Bi–Y, Y–Nb and Bi-doped Y–Nb oxides at moderate temperatures

D.A. Bayot, A.M. Dupont and Michel M. Devillers

Page 1141

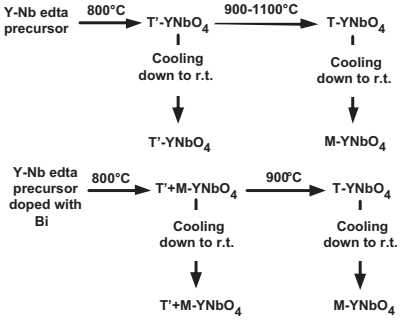

Bi–Y, Nb–Y and Bi-doped Nb–Y oxides were prepared by a molecular precursors method from pre-isolated water-soluble edta-based complexes. The cubic $Bi_{1-x}Y_xO_{1.5}$ and Y_3NbO_7 oxides were obtained in a pure form at the moderate temperature of 650 °C. A distorted tetragonal $YNbO_4$ phase was also stabilized at room temperature by calcining the precursor at 800 °C, and the pure corresponding monoclinic oxide has been obtained near 1100 °C.

Hydrothermal synthesis and crystal structure of the $Ni_2(C_4H_4N_2)(V_4O_{12})(H_2O)_2$ and $Ni_3(C_4H_4N_2)_3(V_8O_{23})$ inorganic–organic hybrid compounds. Thermal, spectroscopic and magnetic studies of the hydrated phase

Edurne S. Larrea, José L. Mesa, José L. Pizarro, María I. Arriortua and Teófilo Rojo

Page 1149

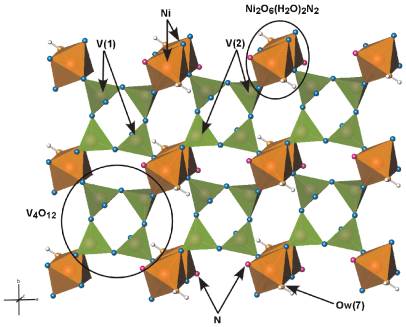

Crystal structure of a sheet of $Ni_2(C_4H_4N_2)(V_4O_{12})(H_2O)_2$.

Rapid Communications

Thermoelectric properties of Ag-doped n-type $(Bi_2Te_3)_{0.9}$–$(Bi_{2-x}Ag_xSe_3)_{0.1}$ ($x = 0$–0.4) alloys prepared by spark plasma sintering

J.L. Cui, W.J. Xiu, L.D. Mao, P.Z. Ying, L. Jiang and X. Qian

Page 1158

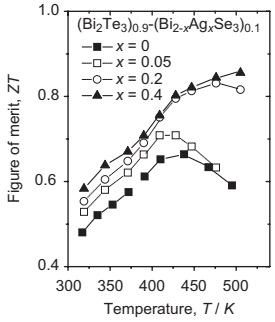

The temperature dependence of dimensionless thermoelectric figure of merit ZT for different $(Bi_2Te_3)_{0.9}$–$(Bi_{2-x}Ag_xSe_3)_{0.1}$ ($x = 0$–0.4) alloys prepared by spark plasma sintering.

Erratum

Erratum to "CONTENTS" [J. Solid State Chem. 179(12) (2006)]

Page 1163